Calculation of Rate Constants for Proton Transfer between Tethered Oxygens

Boonchuan Immaraporn and Alan D. Isaacson*

Department of Chemistry and Biochemistry, Miami University, Oxford, Ohio 45056

Received: August 20, 1997; In Final Form: October 24, 1997[⊗]

To model proton transfer in biological systems, we consider a modified $H_5O_2^+$ system, in which each of the two outermost hydrogens (H*) is assigned a large mass in order to represent a backbone. For the potential energy surface of our model, we add a harmonic function, called the "backbone term", to the potential energy function of Ojamäe, Shavitt, and Singer for $H_5O_2^+$. This backbone term holds the H* atoms apart and, thus, provides various oxygen−oxygen distances and barriers for proton transfer. Variational transition-state theory (CVT) rate constants converge for H* masses greater than 1000 amu. These rate constants decrease exponentially as the backbone−backbone equilibrium distance increases. CVT rate constants also decrease as the backbone-term force constant increases and converge in the limit of a large backbone-term force constant. Tunneling effects are more important at low temperature and for larger values of backbone-term force constants or backbone−backbone equilibrium distances. The motion of the system along the minimum energy path from the saddle point to the product involves the motion of the proton between two relatively fixed oxygens followed by fragment motion and relaxation into the product well.

1. Introduction

Proton transfer is a fundamentally important process in both chemistry and biology. For example, the biological mechanisms of carbonic anhydrase,[1,2] histidine decarboxylase,[3] bovine plasma amine oxidase,[4] alcohol dehydrogenase,[4,5] and bacteriorhodopsin[6−9] are all thought to involve proton-transfer processes. In a biological system, proton transfer can occur by the migration of a proton through the medium, such as water, or by the direct transfer of a proton between two large molecules or membranes. Also, proton transfers between polypeptides and bases in the gas phase[10−12] and between water molecules in acidic solutions[13,14] are of interest to chemists. Here, we consider direct gas-phase proton transfer between protein chains or within the backbone of a macromolecule.

In this work, we model a proton-transfer reaction between two heteroatoms in biological systems. In particular, we calculate the rate constants for gas-phase proton transfer between two hydrogen-bonded hydroxyl groups attached to different macromolecules or to different regions of the same macromolecule, as shown in Figure 1. In our model, the backbone regions of the macromolecule(s) are replaced with single hydrogen atoms with a variable mass (H*). Thus, our model is chemically equivalent to studying proton transfer in $H_5O_2^+$, for which a large number of theoretical studies have been performed.[13−20] Note that in our model, the proton is transferred between oxygens attached to hydrogens. However, in a biological system, each oxygen is bonded to a carbon atom of the backbone. The experimental force constants for these bonds are somewhat different: 5.42 mdyn/Å for the C−O bond in methanol and 8.45 mdyn/Å for the O−H bond in water.[21] In addition, the C−O equilibrium bond distance in methanol is 1.42 Å and the O−H equilibrium bond distance in water is 0.96 Å.[21] Thus, the major difference in using an O−H bond instead of a C−O bond for the H*−O interaction is that the oxygen atom is held somewhat more tightly and about 0.5 Å closer to the backbone.

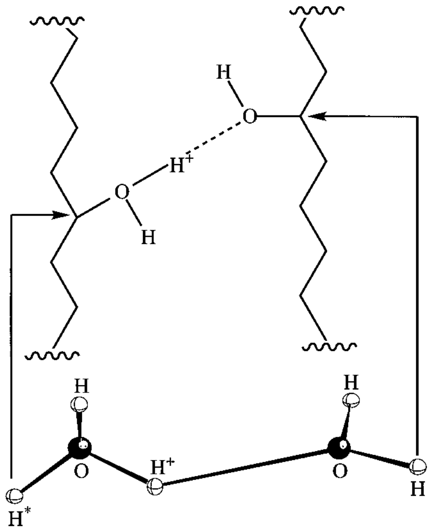

Figure 1. Schematic diagram for the proton-transfer model considered here.

Under the Born−Oppenheimer approximation, the dynamical behavior of the $H_5O_2^+$ system is determined by the total electronic energy as a function of the nuclear coordinates, i.e., the potential energy surface. Fortunately, several potential energy surfaces for $H_5O_2^+$ are available.[13,18−20] The potential energy surface we use here was developed by Ojamäe et al.[14,20] An important feature of this and most other surfaces for the $H_5O_2^+$ system is a global minimum with an O−O distance of approximately 2.4 Å and a proton midway between the oxygens. Hence, in the equilibrium configuration of $H_5O_2^+$, a proton is shared equally between the two water molecules. To represent proton transfer between hydroxyl groups attached to macromolecular backbones, the potential energy surface for our model is obtained from that of $H_5O_2^+$ by adding a "backbone term" that holds the H*'s apart. This backbone term is taken to be a

---

[⊗] Abstract published in *Advance ACS Abstracts,* December 15, 1997.

S1089-5639(97)02722-9 CCC: $15.00

TABLE 1: Barrier Heights (in kcal/mol) for Proton Transfer in $H_5O_2^+$ between Fixed Oxygens

R_{O-O} (Å)	ab initio[14]	potential function
2.60	6.5	8.7
2.80	32.8	32.0

harmonic term containing two adjustable parameters, a force constant and an H*−H* equilibrium distance (see below). This force constant governs the rigidity of the backbone-backbone separation, while different H*−H* equilibrium distances result in different oxygen−oxygen distances; this leads to different barrier heights for proton transfer. We note that an extra harmonic term has been used together with ab initio electronic energies in studies of the potential energy surfaces for the $H_5O_2^+$, $H_4O_2Li^+$, and $H_3O_2^-$ systems by Kar and Scheiner.[22] We further note that the use of an extra harmonic function in the potential energy surface is similar to the technique employed in two studies of proton transfer in water molecule chains.[23,24] Those authors maintained the linearity of the water chain by placing the whole system in a cylindrical harmonic restoring potential, in which harmonic terms were connected to each of the oxygens.

In real systems, proton-transfer reactions might occur for various backbone−backbone interactions and for various distances between donor and acceptor functional groups. Thus, the major goal of the present work is to study the dependences of the proton-transfer rate constant on the distance and rigidity of the H*−H* separation. In section 2, we discuss the methods used in this study, and the results are presented in section 3. Section 4 summarizes our conclusions.

2. Theory and Computational Methods

The potential energy function we use for $H_5O_2^+$ was developed by Ojamäe et al.[14,20] by fitting a functional form to a large number of ab initio points computed at the MP2 level with an aug′-cc-pVTZ basis set. The functional form consists of two-body interactions, three-body interactions, and electrostatic contributions. Although the ab initio calculations are high level, the fit is not quantitatively accurate. For example, the energy barriers to proton transfer for two different fixed oxygen−oxygen distances evaluated from the ab initio data and the fitted potential energy function are compared in Table 1. For these calculations, the starting geometry was obtained from the optimized MP2 geometry by varying the O−O distance. The proton-transfer process was then assumed to occur along the O−O vector, and the O−H−O bond angle was restricted to be linear. While the barriers obtained from the potential energy function and the ab initio data are in good agreement for an O−O distance of 2.80 Å, the results differ by 34% for an O−O distance of 2.60 Å. Nevertheless, we are confident that the basic topology of the fitted potential energy function is correct, so it should describe the $H_5O_2^+$ electronic energy well enough for the present model. As discussed above, to model our tethered-oxygen system, we add a harmonic term, called the "backbone term", to the $H_5O_2^+$ potential energy function:

$$V_{\mathrm{model}} = V_{H_5O_2^+} + {}^1/_2 k_b (R_{H^*H^*} - R_b)^2 \qquad (1)$$

where k_b is the backbone-term force constant and R_b is the backbone-term H*−H* equilibrium distance. In the present study, we have employed parameter values of 1.0−64.0 mdyn/Å for k_b and 4.130−4.830 Å for R_b. In addition, we have varied m(H*), the atomic mass of H*, from 10 to 10 000 amu.

Proton-transfer rate constants were obtained for various sets of backbone-term parameters and H* masses using several levels of transition-state theory. In conventional transition state theory (TST),[25−27] the rate constant at temperature T for the unimolecular reaction in the present work is given by

$$k^{\mathrm{TST}}(T) = \frac{k_B T}{h}\frac{Q^{\ddagger}(T)}{Q_A(T)}\exp(-V^{\ddagger}/k_B T) \qquad (2)$$

where k_B is Boltzmann's constant, h is Planck's constant, $V^{\ddagger}$ is the classical potential energy of the saddle point relative to the energy of the hydrogen-bonded reactant at its equilibrium geometry, $Q_A(T)$ is the partition function of the reactant, and $Q^{\ddagger}(T)$ is the transition-state partition function at the saddle point. (In this work, the bound vibrational and rotational motions were assumed to be separable, and the vibrational partition functions were computed quantum mechanically within the harmonic approximation.) An improved version of TST, called canonical variational transition-state theory (CVT),[28−30] yields more accurate rate constants by optimizing the location of the dividing hypersurface. By locating the dividing hypersurface at the reaction "bottleneck", CVT minimizes recrossing effects. The unimolecular CVT rate constant is given by

$$k^{\mathrm{CVT}}(T) = \min_s \frac{k_B T}{h}\frac{Q^{\mathrm{GT}}(T,s)}{Q_A(T)}\exp[-V_{\mathrm{MEP}}(s)/k_B T] \qquad (3)$$

where $V_{\mathrm{MEP}}(s)$ is the classical potential energy at a point on the minimum energy path (MEP) corresponding to reaction-coordinate value s, and $Q^{\mathrm{GT}}(T,s)$ is the generalized transition-state partition function at s. Exploration of the MEP is performed by a steepest-descents method in mass-scaled coordinates.[29] For chemical reactions involving the transfer of a hydrogen atom, quantum effects should not be neglected. In the present work, these effects are included by multiplying the CVT rate constant by transmission coefficients obtained from semiclassical approaches developed by Truhlar et al.:[30−38]

$$k^{\mathrm{CVT/G}}(T) = \kappa^{\mathrm{CVT/G}}(T)\, k^{\mathrm{CVT}}(T) \qquad (4)$$

where $\kappa^{\mathrm{CVT/G}}$ is given by

$$\kappa^{\mathrm{CVT/G}}(T) = \frac{\exp[V_a(s_*^{\mathrm{CVT}}(T))/k_B T]}{k_B T}\int_0^{\infty} P^{\mathrm{SAG}}(E)\exp(-E/k_B T)\,\mathrm{d}E \qquad (5)$$

where $s_*^{\mathrm{CVT}}(T)$ is the location of the CVT transition state for temperature T. These methods assume that tunneling occurs through the ground state vibrationally adiabatic potential energy curve, $V_a(s)$, which is obtained by the addition of the generalized transition state zero-point energy to the classical energy along the MEP:

$$V_a(s) = V_{\mathrm{MEP}}(s) + \sum_{m=1}^{F-1}\epsilon_{\mathrm{VIB,m}}(n_m = 0, s) \qquad (6)$$

where $\epsilon_{\mathrm{VIB,m}}$ ($n_m = 0,s$) is the vibrational zero-point energy of generalized bound normal mode m. Here $P^{\mathrm{SAG}}(E)$ is the semiclassical ground-state probability of tunneling through $V_a(s)$ at total energy E. In the minimum-energy-path semiclassical adiabatic ground-state method (MEPSAG),[30−32] the tunneling path is assumed to lie along the MEP. For cases in which the curvature of the reaction path is significant, inclusion of this effect leads to the small-curvature semiclassical adiabatic

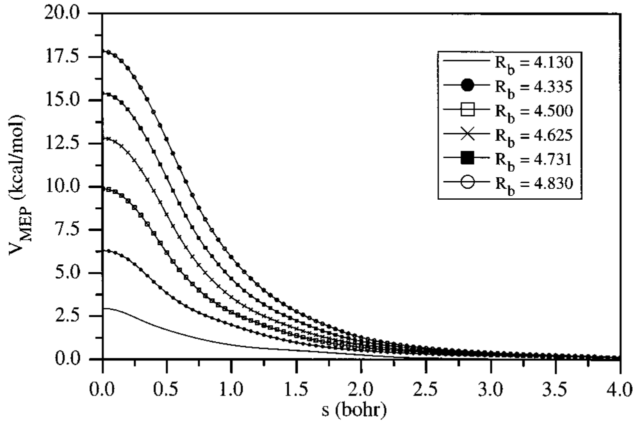

Figure 2. Classical potential energy (V_{MEP}) for $k_b = 8.0$ mdyn/Å and $R_b = 4.130$, 4.335, 4.500, 4.625, 4.731, and 4.830 Å as functions of reaction coordinate s relative to the energy of the reactant for that R_b value.

ground-state approach (SCSAG).[30,33] The SCSAG method generally predicts a larger tunneling contribution than the MEPSAG method does. When the curvature coupling to the reaction path is significant in more than one bound mode, a modified version of the SCSAG method, called the centrifugal-dominant small-curvature semiclassical adiabatic ground-state approach (CD-SCSAG)[34] is recommended. All the calculations presented in this work were performed with the POLYRATE 4.0 program.[34]

3. Results and Discussion

We computed the minimum energy path (MEP) for different backbone-term parameters and H* masses by a steepest-descents method in mass-scaled coordinates with a step size of 0.0001 bohr, where the coordinates are scaled to a reduced mass of 1 amu. This provides the system geometry and classical energy, $V_{MEP}(s)$, relative to that of the reactant, as functions of the reaction coordinate, s. At every 0.01 bohr along the MEP, we performed a projected normal-mode analysis[39] and obtained the ground-state vibrationally adiabatic energy, $V_a(s)$, of the system. Note that, while the potential energy surface is insensitive to the H* mass, the MEP and, hence, the $V_{MEP}(s)$ and $V_a(s)$ curves, depend on m(H*). Unless explicitly stated otherwise, we have chosen m(H*) = 10 000 amu for the results presented below. Note also that the reaction path is symmetric: the reactant and product are equivalent, and the saddle point lies midway between them. Therefore, we need to discuss only that portion of the reaction path from the saddle point ($s = 0$) to the product ($s > 0$). Figure 2 displays $V_{MEP}(s)$ for $k_b = 8.0$ mdyn/Å and $R_b = 4.130$, 4.335, 4.500, 4.625, 4.731, and 4.830 Å as functions of the reaction coordinate, s. This figure shows that the barrier height and width increase dramatically as R_b increases. This is consistent with the relationship between the barrier height and the distance between proton-donor and -acceptor groups reported by Scheiner.[40] To understand this behavior, that author assumed that the proton-transfer process can be decomposed into two simultaneous separate processes: the bond dissociation of the proton from the donor and the bond formation of the proton with the acceptor. Qualitatively, the sum of the potentials of these two processes should give the proton-transfer potential, the maximum of which comes from the summation of the energies at the crossing point of these two potentials. Based on this argument, Scheiner reasoned that the longer the distance between proton donor and acceptor groups, the higher the intersection of these two potentials, and hence, the higher the barrier. The same trend is also observed in Figure 3, which shows $\Delta V_a(s)$, i.e., the difference between $V_a(s)$ and the ground-state vibrationally adiabatic energy of the reactant, for $k_b = 8.0$ mdyn/Å and the same set of R_b values as functions of the reaction coordinate. In fact, the presence of both classical and adiabatic barriers is mostly determined by R_b. Generally, there is no barrier for $R_b < 4.1$ Å ($R_{O-O} < 2.5$ Å); for $k_b \geq 1$ mdyn/Å, there is a barrier for $R_b > 4.1$ Å. We note that the present classical and adiabatic barrier heights for $k_b = 8.0$ mdyn/Å and $R_b = 4.500$ Å (9.89 and 6.36 kcal/mol, respectively) are similar to, although somewhat larger than the corresponding MP2 values obtained by Kar and Scheiner[22] with a 6-31+G** basis set (8.60 and 4.54 kcal/mol, respectively). In addition, the present decrease in the classical barrier height for $R_b < 4.500$ Å is less pronounced than that observed by those authors. Along the reaction path, we often found one or more regions where a normal mode orthogonal to the reaction path has a double-well potential and, therefore, an imaginary frequency at the MEP. These modes were ignored for the calculations in these regions. However, these modes affect the shape of $V_a(s)$ by creating local minima along the reaction path, as shown in Figure 3. For example, for $k_b = 8.0$ mdyn/Å and $R_b = 4.500$ Å, imaginary-frequency regions along the reaction path toward the product side occur for s between 0.18 and 0.90 bohr and for s between 1.43 and 2.54 bohr. The former explains the sharp decrease in $V_a(s)$ for s around 0.70 bohr. In this region, the imaginary-frequency mode corresponds to O−H−O inversion. As we continue to move along the reaction path, the frequency of this mode once again becomes real, and $V_a(s)$ increases from the contribution of this mode. After passing the local maximum ($s \cong 1.1$ bohr), $V_a(s)$ drops rapidly in part because the mode corresponding to O−H−O inversion again has an imaginary frequency.

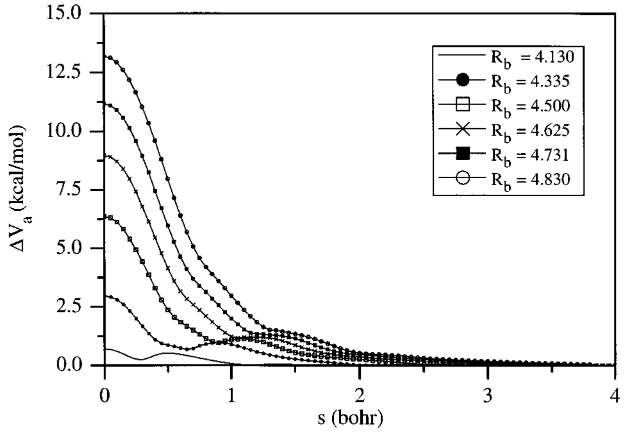

Figure 3. Ground-state vibrationally adiabatic potential energy (ΔV_a) for $R_b = 4.130$, 4.335, 4.500, 4.625, 4.731, and 4.830 Å and $k_b = 8.0$ mdyn/Å as functions of reaction coordinate s relative to the adiabatic energy of the reactant for that R_b value.

In Figure 4, $V_{MEP}(s)$ is plotted for $R_b = 4.830$ Å and $k_b = 1.0$, 2.0, 4.0, 8.0, 16.0, 32.0, and 64.0 mdyn/Å. While the k_b force constant has a small effect on reactant and product properties, it significantly affects the properties of the system at the saddle point and along the reaction path. In fact, the classical barrier height increases rapidly as k_b increases from 1.0 to 4.0 mdyn/Å. For $k_b \geq 8.0$ mdyn/Å, the barrier height increases slowly toward a large-k_b limit. We also note that $V_{MEP}(s)$ decreases to zero more rapidly for larger k_b values. To explain these observations, we note that a smaller value of k_b leads to a less rigid system and allows the oxygen atoms to move more during the proton-transfer process. In particular, a

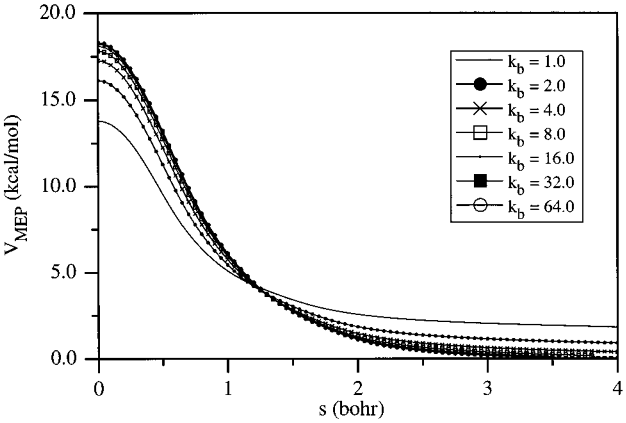

Figure 4. Classical potential energy (V_{MEP}) for R_b = 4.830 Å and k_b = 1.0, 2.0, 4.0, 8.0, 16.0, 32.0, and 64.0 mdyn/Å as functions of reaction coordinate *s* relative to the energy of the reactant for that k_b value.

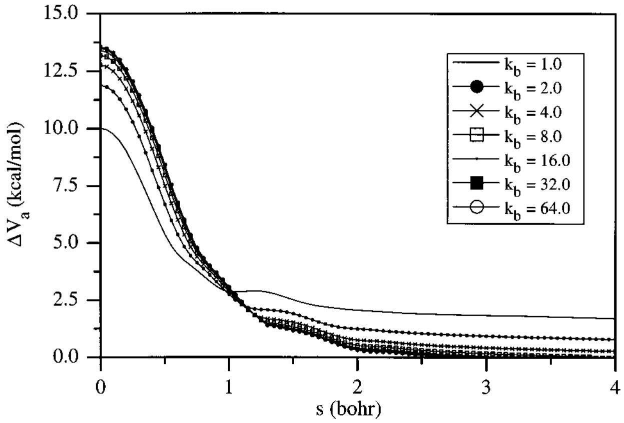

Figure 5. Ground-state vibrationally adiabatic potential energy (ΔV_a) for k_b = 1.0, 2.0, 4.0, 8.0, 16.0, 32.0, and 64.0 mdyn/Å and R_b = 4.830 Å as functions of reaction coordinate *s* relative to the adiabatic energy of the reactant for that k_b value.

greater shortening of the O—O distance at the saddle point for smaller values of k_b leads to a lower barrier height, as discussed below. Similar trends are observed for $\Delta V_a(s)$, as shown in Figure 5.

For R_b = 4.830 Å and k_b = 64.0 mdyn/Å, the geometrical changes as the system proceeds along the reaction path from the saddle point toward the product are displayed in Figure 6. From this figure, we see that the proton first moves from one oxygen to the other, followed by the bending of H—O—H angles in the H_3O^+ moiety. The system then relaxes into the product well by twisting around the O—H—O bond axis. The oxygen—oxygen (O—O) and donor oxygen—proton (O—H^+) distances are also plotted as functions of *s* for this set of backbone-term parameters in Figure 7. Between *s* = 0 and *s* = 0.7 bohr, the O—O distance remains nearly constant as the O—H^+ distance increases, corresponding to a direct proton transfer between fixed oxygens, in qualitative agreement with the behavior observed in an ab initio study of this system by Kar and Scheiner.[22] The changes in these curves for larger values of *s* correspond to the other motions described above. The same kinds of motion are observed for smaller values of k_b, except that the relaxation process involves some other types of motion, e.g., O—H—O bending along with twisting around the O—H—O bond axis. This leads to a longer reaction path, as shown in Figures 4 and 5. We note for the calculation of the rate constants that the saddle-point geometry has a C_2 axis bisecting the O—H—O angle. This gives a factor of one-half in the transition state rotational partition function.

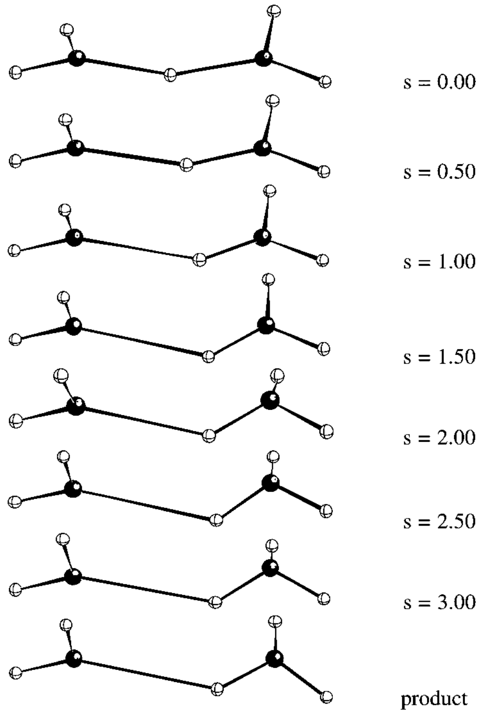

Figure 6. Geometrical changes along the proton-transfer reaction path from the saddle point (*s* = 0 bohr) to the product for k_b = 64.0 mdyn/Å and R_b = 4.830 Å.

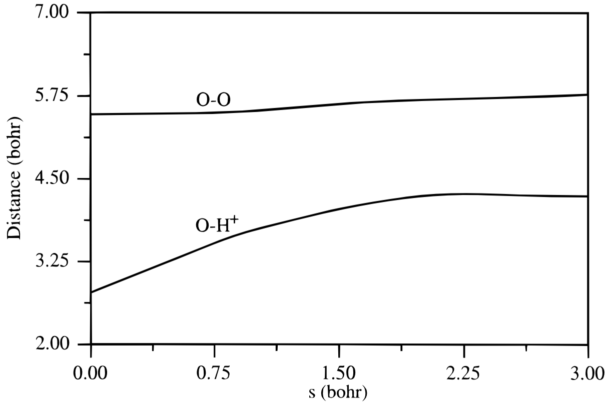

Figure 7. Oxygen—oxygen (O—O) and donor oxygen—proton (O—H^+) distances as functions of the reaction coordinate *s* for R_b = 4.830 Å and k_b = 64.0 mdyn/Å.

TABLE 2: Rate Constants (in s^{-1}) for Various H* Masses at 300 K[a]

m(H*) (amu)	TST	CVT	CVT/MEPSAG	CVT/CD-SCSAG
10	2.47(4)	2.47(4)	4.51(5)	1.09(6)
100	1.75(4)	1.75(4)	3.09(5)	7.41(5)
1000	1.67(4)	1.67(4)	2.95(5)	7.08(5)
10000	1.67(4)	1.67(4)	2.94(5)	7.05(5)

[a] k_b = 8.0 mdyn/Å and R_b = 4.731 Å; power of 10 is given in parentheses.

Since we are modeling a proton-transfer reaction between two hydroxyl groups attached to a backbone, we calculated rate constants for H* masses of 10, 100, 1000, and 10 000 amu. The results at 300 K are shown in Table 2 for R_b = 4.731 Å and k_b = 8.0 mdyn/Å. No variational effect is observed here because the variational bottleneck is at the saddle point for this set of backbone-term parameters; hence, both TST and CVT predict the same rate constants. On the other hand, both reaction-path tunneling (CVT/MEPSAG vs CVT) and the

TABLE 3: Mass-Dependent Properties of the Reactant and Saddle Point for Various H* Masses[a]

m(H*) (amu)	$V_a^{\ddagger}$ (kcal/mol)	V_a^{R} (kcal/mol)	$\Delta V_a^{\ddagger}$ (kcal/mol)	$I_A^{\ddagger}I_B^{\ddagger}I_C^{\ddagger}/I_A^{R}I_B^{R}I_C^{R}$
10	41.219	30.281	10.938	0.745
100	38.374	27.231	11.143	0.721
1000	37.697	26.526	11.171	0.714
10000	37.517	26.343	11.174	0.713

[a] $k_b = 8.0$ mdyn/Å and $R_b = 4.731$ Å.

incorporation of reaction-path curvature (CVT/CD-SCSAG vs CVT/MEPSAG) are significant for all H* masses. For all backbone-term parameters, both CVT and CVT/CD-SCSAG rate constants decrease as the H* mass increases, and they converge for an H* mass of approximately 1000 amu. To understand these trends, the mass-dependent quantities in the TST rate constant (see eq 2), i.e., the ground-state vibrationally adiabatic potential energy of the reactant, V_a^R, and of the saddle point, $V_a^{\ddagger}$, the adiabatic barrier height, $\Delta V_a^{\ddagger}$, and the ratio of the product of the three principal moments of inertia at the saddle point to that of the reactant, $I_A^{\ddagger}I_B^{\ddagger}I_C^{\ddagger}/I_A^{R}I_B^{R}I_C^{R}$, are listed in Table 3 for the same set of backbone-term parameters as in Table 2. From this table, we note that $\Delta V_a^{\ddagger}$ increases as the H* mass increases. This is because V_a^R decreases more rapidly than $V_a^{\ddagger}$ does as the H* mass increases. The increase in $\Delta V_a^{\ddagger}$ leads to the decrease in the predicted rate constants between m(H*) values of 10 and 1000 amu. For large H* masses, the decrease in V_a^R for increasing m(H*) is almost the same as that in $V_a^{\ddagger}$, and the moment of inertia ratio is relatively constant. These result in the convergence of the predicted rate constants for $m(\text{H*}) \geq 1000$ amu. Since, in our model, the H* atom represents the backbone of a very large molecule, we have taken the value of m(H*) to be 10 000 amu in the rest of the calculations presented herein.

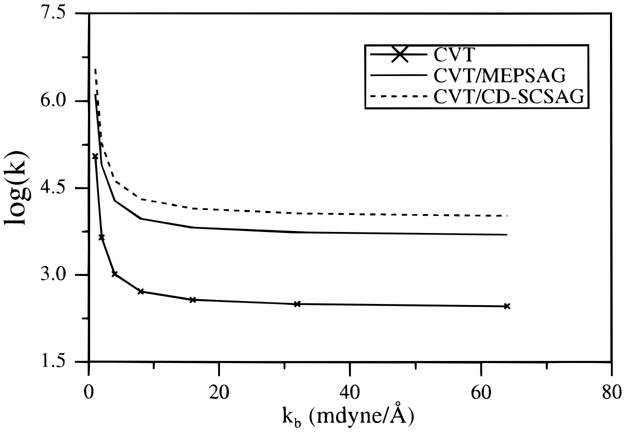

Figure 8. Logarithm of the rate constants at 300 K as functions of k_b for $R_b = 4.830$ Å.

TABLE 5: CVT Rate Constants and Transmission Coefficients at 300 K and Saddle-Point Oxygen−Oxygen Distances (R_{O-O}) for Various k_b Values[a]

k_b (mdyn/Å)	R_{O-O} (Å)	k^{CVT} (s^{-1})	κ^{MEPSAG}	$\kappa^{CD-SCSAG}$
1.0	2.638	5.46(6)	7.88	18.9
2.0	2.715	1.78(5)	13.3	36.1
4.0	2.763	3.58(4)	16.4	41.5
8.0	2.790	1.67(4)	17.6	42.4
16.0	2.803	1.15(4)	18.1	42.4
32.0	2.810	9.54(3)	18.2	42.4
64.0	2.813	8.71(3)	18.3	42.3

[a] $R_b = 4.731$ Å; power of 10 is given in parentheses.

The backbone term in our model potential energy function represents the potential energy of a “spring” that holds the two H* atoms apart. For $k_b = 8.0$ mdyn/Å and $m(\text{H*}) = 10\,000$ amu, this term yields a frequency of about 50 cm^{-1} for the H*−H* stretch. We have already noted how the backbone-term force constant, k_b, affects the $V_{MEP}(s)$ and $V_a(s)$ curves. This force constant also affects the proton-transfer rate constant and other dynamical properties, because it determines the overall flexibility of the system, as discussed below. CVT, CVT/MEPSAG, and CVT/CD-SCSAG rate constants at 200, 300, and 400 K for k_b values from 1.0 to 64.0 mdyn/Å and R_b values from 4.130 to 4.830 Å are listed in Table 4S in the Supporting Information. We note that there is a variational effect (CVT vs TST) only for $R_b = 4.130$ Å and $k_b = 1.0$ mdyn/Å and for $R_b = 4.500$ Å and $k_b = 1.0$ mdyn/Å. This results in increases in some of the predicted rate constants as k_b changes from 1.0 to 2.0 mdyn/Å for these R_b values. A logarithmic plot of the predicted rate constants at 300 K vs k_b for $R_b = 4.830$ Å is also shown in Figure 8. These rate constants computed both without and with the inclusion of reaction-path tunneling decrease very quickly for k_b values between 1 and 8 mdyn/Å, while for higher k_b values, the rate constants approach a high-k_b limit. To understand these results in more detail, the CVT rate constant and transmission coefficients at 300 K and the saddle-point oxygen−oxygen distance for $R_b = 4.731$ Å and various k_b values are shown in Table 5. All of these properties tend toward a large-k_b limit. The reason for this is that for a large k_b value, the H*−H* distance, and hence, the O−O distance, remains nearly constant all along the reaction path. However, for a small k_b value, the system is more flexible, and the oxygens move closer together at the saddle point during the proton-transfer process, as is evident from Table 5. Similar behavior was observed in an ab initio study of this system by Kar and Scheiner.[22] This leads to lower proton-transfer barriers and larger predicted rate constants for smaller k_b values. Tunneling effects also play an important role in the dynamical behavior of the system, especially at low temperature and for large k_b values. The CD-SCSAG method predicts more tunneling than the MEPSAG method for all k_b values. This is expected because of the effects of reaction-path curvature. Tunneling contributions from energies below 2.5 kcal/mol are no larger than 8% for all the k_b values studied here. Thus, by considering only the shapes of the $V_a(s)$ curves in Figure 5 above an energy of 2.5 kcal/mol, we might expect larger transmission coefficients for smaller k_b values. However, the exponential factor, $\exp[V_a(s_*^{CVT}(T))/k_BT]$, in the transmission coefficient (see eq 5) is larger for a higher adiabatic barrier. This factor offsets the Boltzmann average of the tunneling probability, $P^{SAG}(E)$, in the large-k_b transmission coefficients, yielding larger transmission coefficients for *larger* k_b values. We note that for $k_b = 1.0$ and 2.0 mdyn/Å and $R_b = 4.130$ Å, the transmission coefficients are less than one (see Table 4S). This results from the fact that, for these sets of backbone-term parameters, the adiabatic energy at the CVT transition state lies below the maximum of the ground-state vibrationally adiabatic curve, V^{AG}. To correct the MEPSAG and CD-SCSAG transmission coefficients for the contributions from tunneling energies that lie between $V_a(s_*^{CVT}(T))$ and V^{AG}, an additional factor, called the classical adiabatic ground-state (CAG)[32] transmission coefficient, is included in the MEPSAG and CD-SCSAG rate constants, making them smaller than the CVT rate constant in these cases. In summary, we find that the more flexible the system (i.e., the smaller the k_b value), the faster the proton-transfer reaction. When the system is very rigid, the effects of tunneling are expected to play a more important role in the dynamical behavior.

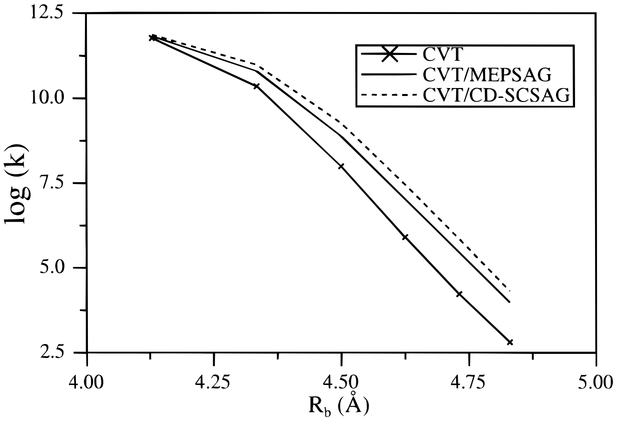

Figure 9. Logarithm of the rate constants at 300 K as functions of R_b for $k_b = 8.0$ mdyn/Å.

TABLE 6: CVT Rate Constants and Transmission Coefficients at 300 K and Saddle-Point Oxygen−Oxygen Distances (R_{O-O}) for Various R_b Values[a]

R_b (Å)	R_{O-O} (Å)	k^{CVT} (s^{-1})	κ^{MEPSAG}	$\kappa^{CD-SCSAG}$
4.130	2.486	9.29(11)	1.04	1.08
4.335	2.527	8.93(10)	1.76	2.22
4.500	2.592	2.64(9)	4.55	8.54
4.625	2.652	1.01(7)	8.84	22.3
4.731	2.716	1.78(5)	13.3	36.1
4.830	2.787	4.47(3)	17.5	42.3

[a] $k_b = 2.0$ mdyn/Å; power of 10 is given in parentheses.

We now consider the effect of the R_b parameter in the backbone term on the predicted rate constants listed in Table 4S. Figure 9 contains plots of log(k) at 300 K vs R_b for $k_b = 8.0$ mdyn/Å. This figure shows that the CVT rate constant decreases rapidly with increasing R_b. In fact, log(k) decreases nearly linearly with R_b for $R_b \geq 4.335$ Å. Similar trends are observed for the CVT/MEPSAG and CVT/CD-SCSAG rate constants. However, the CVT/MEPSAG and CVT/CD-SCSAG rate constants do not decrease quite as rapidly as the CVT rate constants with increasing R_b because of the effects of reaction-path tunneling, as discussed below. Rate constants for other backbone-term force constants exhibit similar behavior. As shown in Figures 2 and 3, a larger R_b value leads to higher barriers in the $V_{MEP}(s)$ and $V_a(s)$ curves. This explains the observed decrease in the CVT rate constant as the R_b value increases. We might also expect the transmission coefficients to be smaller for a larger $V_a(s)$ barrier. However, as noted above, the $\exp[V_a(s_*^{CVT}(T))/k_BT]$ factor in the transmission coefficient is also large when the $V_a(s)$ barrier is high and actually leads to an *increasing* transmission coefficient for increasing R_b in this case. This is demonstrated in Table 6, which lists CVT rate constants and transmission coefficients at 300 K and saddle-point O−O distances for various R_b values for $k_b = 2.0$ mdyn/Å. The increases in the transmission coefficients for increasing R_b partly offset the dramatic decrease in the CVT rate constant factor in the CVT/MEPSAG and CVT/CD-SCSAG rate constants for increasing R_b values. Therefore, the effects of reaction-path tunneling are predicted to be most important for large R_b values and low temperature. As expected, the CD-SCSAG method yields larger transmission coefficients than those from the MEPSAG method. Furthermore, a larger R_b value leads to a larger H*−H* separation; hence, the O−O distance at the saddle point also increases with increasing R_b. Our model indicates that the proton-transfer process occurs most rapidly for small O−O distances, e.g., around 2.5 Å, where tunneling is not significant. However, for larger O−O distances, tunneling is expected to be very important.

4. Summary

In this work, we have studied a highly idealized model for symmetric proton transfer between oxygens attached to molecular backbones. Canonical variational transition state theory (CVT) has been used to compute proton-transfer rate constants. The potential energy surface we have used is a combination of that of Ojamäe et al.[14,20] for $H_5O_2^+$ and an extra harmonic "backbone term". The key parameters of the model are the mass of the backbone, the oxygen−oxygen distance, and the flexibility of the system. The latter two are controlled by the backbone term.

The predicted rate constants were found to converge for a backbone mass of 1000 amu. As expected, we found that the energy barrier to proton transfer is dependent upon the backbone−backbone distance, as this affects the oxygen−oxygen (O−O) distance at the saddle point. Specifically, we found that there is a barrier to proton transfer for a backbone−backbone distance greater than 4.1 Å, corresponding to a minimum saddle-point O−O distance of 2.5 Å, which is shorter than typical distances between heteroatoms involved in hydrogen bonding in proteins and other large molecules.[41] In addition, a larger saddle point O−O distance leads to a higher barrier; this, in turn, leads to a nearly exponential decrease in the predicted rate constant. In general, the predicted rate constant at room temperature decreases by 6−9 orders of magnitude as the backbone−backbone distance parameter increases from 4.13 to 4.83 Å. The predicted rate constants were also found to increase as the degree of rigidity of the system decreases, as this leads to a shorter O−O distance at the saddle point and, thus, to a lower barrier. Hence, our model indicates that the proton-transfer process is more rapid for shorter backbone−backbone distances or more flexible backbone−backbone interactions. In addition, tunneling effects were found to be most important for a high degree of rigidity, for a large backbone-backbone separation, and for low temperature. Finally, the proton-transfer process described by our model was found to consist of three nearly distinct phases: motion of the fragments from the hydrogen-bonded reactant geometry to the saddle-point fragment geometry, proton transfer from the donor oxygen to the acceptor oxygen with a relatively fixed O−O distance, and motion of the fragments to the hydrogen-bonded product geometry. Further investigations involving alternate treatments for the imaginary-frequency normal modes orthogonal to the MEP and for incorporating the high degree of reaction-path curvature in the calculation of the transmission coefficients are currently in progress. We are confident that this work provides greater insight into direct proton-transfer processes in biological systems and demonstrates the utility of the present model for the description of other, e.g., nonsymmetric, proton-transfer reactions.

Acknowledgment. The authors are grateful to Dr. Steve Scheiner for suggesting the ideas used in the model presented here and to Dr. Lars Ojamäe for providing his potential energy surface. All calculations reported here were carried out on the Miami University DEC AlphaServer 2100 computer, and the computer time is greatly appreciated.

Supporting Information Available: Table 4S gives CVT, CVT/MEPSAG, and CVT/CD-SCSAG rate constants at 200, 300, and 400 K for the model proton-transfer process considered herein. Results are listed for $k_b = 1.0, 2.0, 4.0, 8.0, 16.0, 32.0$, and 64.0 mdyn/Å and for $R_b = 4.130, 4.335, 4.500, 4.625, 4.731$, and 4.830 Å (2 pages). Ordering information is given on any current masthead page.

References and Notes

(1) Silverman, D. N.; Lindskog, S. *Acc. Chem. Res.* **1988**, *21*, 30.

(2) Zhang, X.; Hubbard, C. D.; van Eldik, R. *J. Phys. Chem.* **1996**, *100*, 9161.

(3) Rose, I. A.; Kuo, D. J. *Biochemistry* **1992**, *31*, 5887.

(4) Rucker, J.; Cha, Y.; Jonsson, T.; Grant, K. L.; Klinman, J. P. *Biochemistry* **1992**, *31*, 11489.

(5) Ramaswamy, S.; Eklund, H.; Plapp, B. V. *Biochemistry* **1994**, *33*, 5230.

(6) Heberle, J.; Dencher, N. A. Proton transfer in the light-harvesting protein bacteriorhodopsin: An investigation with optical pH-indicators. In *Proton Transfer in Hydrogen-Bonded Systems*; Bountis, T., Ed.; Plenum Press: New York, 1992; pp 187−197.

(7) Birge, R. R.; Govender, D. S. K.; Izgi, K. C.; Tan, E. H. L. *J. Phys. Chem.* **1996**, *100*, 9990.

(8) Muneyuki, E.; Ikematsu, M.; Yoshida, M. *J. Phys. Chem.* **1996**, *100*, 19687.

(9) Ames, J. B.; Ros, M.; Raap, J.; Lugtenburg, J.; Mathies, R. A. *Biochemistry* **1992**, *31*, 5328.

(10) Stephenson, J. L., Jr.; McLuckey, S. A. *J. Am. Chem. Soc.* **1996**, *118*, 7390.

(11) McLuckey, S. A.; Glish, G. L.; Van Berkel, G. J. *Anal. Chem.* **1991**, *63*, 1971.

(12) Cassady, C. J.; Wronka, J.; Kruppa, G. H.; Laukien, F. H. *Rapid Commun. Mass Spectrom.* **1994**, *8*, 394.

(13) Lobaugh, J.; Voth, G. A. *J. Chem. Phys.* **1996**, *104*, 2056.

(14) Ojamäe, L.; Shavitt, I.; Singer, S. J. *Int. J. Quantum Chem. Symp.* **1995**, *29*, 657.

(15) Frisch, M. J.; Del Bene, J. E.; Binkley, J. S.; Schaefer, H. F. III *J. Chem. Phys.* **1986**, *84*, 2279.

(16) Latajka, Z.; Scheiner, S. *J. Mol. Struct. (THEOCHEM)* **1991**, *234*, 373.

(17) Del Bene, J. E.; Shavitt, I. *J. Mol. Struct. (THEOCHEM)* **1994**, *307*, 27.

(18) Stillinger, F. H.; David, C. W. *J. Chem. Phys.* **1978**, *69*, 1473.

(19) Halley, J. W.; Rustad, J. R.; Rahman, A. *J. Chem. Phys.* **1993**, *98*, 4110.

(20) Ojamäe, L.; Shavitt, I.; Singer, S. J., to be published. The specific surface employed here is denoted as oss1 by those authors.

(21) *Handbook of Chemistry and Physics*; Lide, D. R., Ed.; CRC Press: Boca Raton, FL, 1997.

(22) Kar, T.; Scheiner, S. *J. Am. Chem. Soc.* **1995**, *117*, 1344; *Int. J. Quantum Chem. Symp.* **1995**, *29*, 567.

(23) Drukker, K.; Hammes-Schiffer, S. *J. Chem. Phys.* **1997**, *107*, 1.

(24) Pomès, R.; Roux, B. *J. Phys. Chem.* **1996**, *100*, 2519.

(25) Eyring, H. *J. Chem. Phys.* **1935**, *3*, 107.

(26) Glasstone, S.; Laidler, K. J.; Eyring, H. *The theory of rate processes*; McGraw-Hill: New York, 1941.

(27) Laidler, K. J. *Theories of chemical reaction rates*; McGraw-Hill: New York, 1969.

(28) Truhlar, D. G.; Garrett, B. C. *Acc. Chem. Res.* **1980,** *13*, 440. Garrett, B. C.; Truhlar, D. G. *J. Chem. Phys.* **1979**, *70*, 1593; **1980**, *72*, 3460; *J. Phys. Chem.* **1979**, *83*, 1079; **1980**, *84*, 682; **1983**, *87*, 4553E; *J. Am. Chem. Soc.* **1979**, *101*, 5207; **1980**, *102*, 2559.

(29) Isaacson, A. D.; Truhlar, D. G. *J. Chem. Phys.* **1982**, *76*, 1380.

(30) Truhlar, D. G.; Isaacson, A. D.; Garrett, B. C. Generalized Transition State Theory. In *Theory of Chemical Reaction Dynamics*; Baer, M., Ed.; CRC Press: Boca Raton, FL, 1985; Vol. 4, pp 65−137.

(31) Garrett, B. C.; Truhlar, D. G. *J. Phys. Chem.* **1979**, *83*, 2921.

(32) Garrett, B. C.; Truhlar, D. G.; Grev, R. S.; Magnuson, A. W. *J. Phys. Chem.* **1980**, *84*, 1730; **1983**, *87*, 4554E.

(33) Skodje, R. T.; Truhlar, D. G.; Garrett, B. C. *J. Phys. Chem.* **1981**, *85*, 3019; *J. Chem. Phys.* **1982**, *77*, 5955.

(34) Lu, D.-h.; Truong, T. N.; Melissas, V. S.; Lynch, G. C.; Liu, Y.-P.; Garrett, B. C.; Steckler, R.; Isaacson, A. D.; Rai, S. N.; Hancock, G. C.; Lauderdale, J. G.; Joseph, T.; Truhlar, D. G. *Comput. Phys. Commun.* **1992**, *71*, 235.

(35) Garrett, B. C.; Joseph, T.; Truong, T. N.; Truhlar, D. G. *Chem. Phys.* **1989**, *136*, 271.

(36) Garrett, B. C.; Truhlar, D. G. *J. Chem. Phys.* **1983**, *79*, 4931.

(37) Garrett, B. C.; Truhlar D. G.; Wagner, A. F.; Dunning, T. H., Jr. *J. Chem. Phys.* **1983**, *78*, 4400.

(38) Bondi, D. K.; Connor, J. N. L.; Garrett, B. C.; Truhlar, D. G. *J. Chem. Phys.* **1983**, *78*, 5981.

(39) Miller, W. H.; Handy, N. C.; Adams, J. E. *J. Chem. Phys.* **1980**, *72*, 99.

(40) Scheiner, S. *Acc. Chem. Res.* **1985**, *18*, 174.

(41) Jeffrey, G. A. *An Introduction to Hydrogen Bonding*; Oxford University: New York, 1997.